From Poison to Promotor: Spatially Isolated Metal Sites in Supported Rhodium Sulfides as Hydroformylation Catalysts

Arjun Neyyathala, Edvin Fako, Sandip De,* Daria Gashnikova, Florian Maurer, Jan-Dierk Grunwaldt, Stephan A. Schunk, and Schirin Hanf*

The hydroformylation of alkenes is a cornerstone transformation for the chemical industry, central for both functionalizing and extending the carbon backbone of an alkene. In this study, silica-supported crystalline rhodium sulfide nanoparticles are explored as heterogeneous catalysts in hydroformylation reactions, and it is found that Rh_xS_y systems ($x = 17$, $y = 15$ or $x = 2$, $y = 3$ with 1 wt% Rh on SiO_2) greatly outperform metallic Rh nanoparticles. These systems prove to be exceptionally competitive when benchmarked against other cutting-edge catalysts in terms of activity, with $Rh_{17}S_{15}/SiO_2$ being the superior catalyst candidate. By employing local environment descriptors, unsupervised machine learning and density functional theory, the structure-performance relationships are examined. The results highlight that the presence of S in close proximity to the catalytic site unlocks the tunability of the surface catalytic properties. This allows for the substrate affinity to be modulated, in particular for $Rh_{17}S_{15}$, with adsorption energies rivalling those of pristine Rh and improved spatial resolution.

1. Introduction

The hydroformylation of alkenes using syngas (CO/H_2) for the synthesis of aldehydes is one of the key industrial chemical transformations, with annual global aldehyde manufacturing exceeding 24 million metric tons year.[1–4] Up to now, homogeneous rhodium-based catalysts are the preferred catalyst technology in the area of hydroformylation catalysts, as rhodium has proven to be the most active metal and the selectivity can in general be tuned via the ligand or the reaction conditions.[5–7] However, the use of a homogeneous catalyst involves significant technical challenges for catalyst separation and recycling to avoid the loss of precious metal.[8] Consequently, heterogenized or heterogeneous rhodium-containing catalysts as alternative candidates for oxo-chemistry, such as anchored Rh complexes on solid supports,[8,9] rhodium in zeolite framework,[10] and rhodium-containing nanoparticles,[11,12] have gained significant research interest in the last decade.

A number of approaches in the field of heterogeneous catalysis pursue the mimicking of the steric and electronic environment of an active metal in homogeneous catalysts through the combination of a noble metal together with another less noble metal or non-metal to form alloys,[11,13–19] intermetallic compounds,[12] or other main-group containing metal phases.[20] In this context, also Rh-based catalyst systems, in the form of supported crystalline nanoparticles, such as Rh-Zn,[12] Rh-Co,[14,21] and Rh-P,[11] have been applied as catalysts for hydroformylation reactions. The superior catalytic performance compared to pure metallic rhodium-based catalyst, in liquid[16] and gas phase hydroformylations[11] was already reported for supported crystalline rhodium phosphides, Rh_2P. Their catalytic activity was attributed to the formation of undercoordinated Rh species on the surface of the crystalline nanoparticles, a motif that can be compared to frustrated single sites in homogeneous catalysis.[8,11] The inherent structural features of Rh_2P contribute to its excellent catalytic activity, but also

A. Neyyathala, S. Hanf
Institute for Inorganic Chemistry
Karlsruhe Institute of Technology
Engesserstr. 15, 76131 Karlsruhe, Germany
E-mail: schirin.hanf@kit.edu

E. Fako, S. De, S. A. Schunk
BASF SE
Carl-Bosch Str. 38, 67056 Ludwigshafen, Germany
E-mail: sandip.de@basf.com

The ORCID identification number(s) for the author(s) of this article can be found under https://doi.org/10.1002/sstr.202400260.

D. Gashnikova, F. Maurer, J.-D. Grunwaldt
Institute for Chemical Technology and Polymer Chemistry
Karlsruhe Institute of Technology
Engesserstr. 18/20, 76131 Karlsruhe, Germany

J.-D. Grunwaldt
Institute of Catalysis Research and Technology
Karlsruhe Institute of Technology
Hermann-von-Helmholtz-Platz 1, 76344 Eggenstein-Leopoldshafen, Germany

S. A. Schunk
hte GmbH, the high throughput experimentation company
Kurpfalzring 104, 69123 Heidelberg, Germany

S. A. Schunk
Institute of Chemical Technology
Faculty of Chemistry and Mineralogy
Leipzig University
Linnéstr. 3, 04103 Leipzig, Germany

the electronic state of rhodium is modulated, leading to optimal weaker CO binding, which has been argued to have a positive influence on the overall activity.[16]

Despite the fact, that sulfur is considered to be a catalyst poison in many cases in catalysis and in general reduces the affinity of the surface toward organic substrates, metal sulfide phases, such as palladium sulfides or rhodium sulfides have been explored as catalysts for the semi hydrogenation of alkynes[22,23] and in the framework of electrocatalysis.[24–26] Also, metal sulfides have been applied in the photocatalytic energy conversion, including H_2 production, CO_2 reduction, and N_2 fixation,[27] in carbonylation reactions[28] as well as in the context of hydrotreating, for example, hydrodesulfurization, catalysis.[29] However, this concept has not been exploited systematically and not at all in the framework of oxo-chemistry. In this work, we thus investigate the use of supported crystalline rhodium sulfide nanoparticles, with a particular focus on the metal-rich $Rh_{17}S_{15}$ and metal-lean Rh_2S_3 phases, toward the use in liquid-phase hydroformylation reactions of alkenes. We demonstrate how rhodium sulfides can be tailored to go beyond emulating the activity of the parent metal with a p-loaded surrogate, by modulating the surface composition of the catalyst and the formation of spatially isolated metal sites to substantially improve on the activity and selectivity in the hydroformylation of alkenes. This study will give general guidelines for the design of highly active heterogeneous single-site catalysts based on a straight-forward d-block/p-block element combination strategy, with profound implications for one of the most important catalytic reactions in the chemical industry.

2. Results and Discussion

2.1. Synthetic Access to Supported Rhodium Sulfide Nanoparticles

The two rhodium sulfide phases selected for this investigation are the metal-rich $Rh_{17}S_{15}$ (Rh/S = 1.13) and the metal-lean Rh_2S_3 (Rh/S = 0.66) phase. The silica-supported rhodium sulfides particles were synthesized using an incipient wetness impregnation method of reactive precursors. Rhodium acetate (Rh(OAc)$_3$) and thiourea (CH$_4$N$_2$S) were dissolved in water and added dropwise to silica (Cariact). The impregnated precursors were subsequently dried and brought to reaction via a thermal treatment in a flowing stream of argon to obtain the supported Rh$_x$S$_y$ phases (**Figure 1**a). There is a loss of volatile sulfur during the thermal treatment, and so the addition of an excess quantity of thiourea is required to enable the Rh$_x$S$_y$ phase formation. Hence, 20, 30 and 50 mol% excess of thiourea with respect to the stoichiometric ratio of the corresponding sulfide,
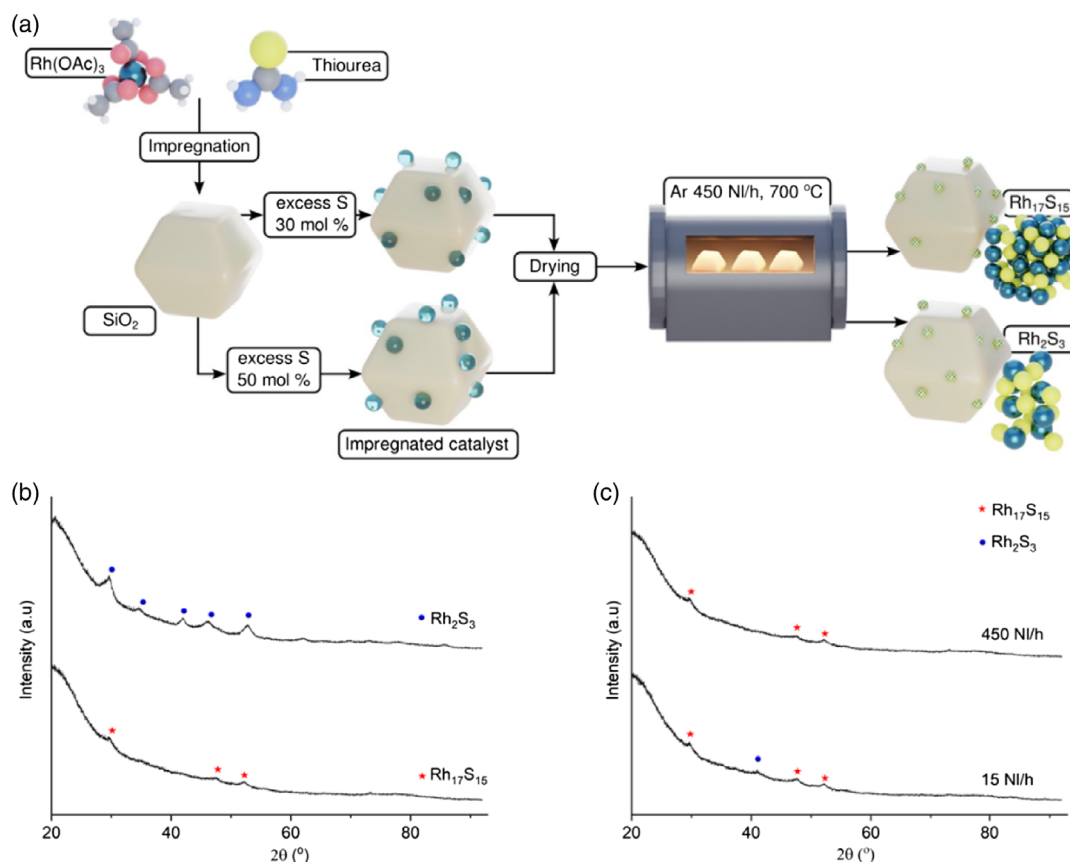

Figure 1. a) Synthetic access to supported nanoparticles of crystalline rhodium sulfides and PXRD patterns of b) Rh$_{17}$S$_{15}$/SiO$_2$ (10 wt% Rh) and Rh$_2$S$_3$/SiO$_2$ (10 wt% Rh), c) products obtained after the thermal treatment at 700 °C of the impregnated precursors for the synthesis of Rh$_{17}$S$_{15}$/SiO$_2$ (10 wt% Rh) using different argon flow rates. •Rh$_2$S$_3$ (ICSD: 56 882, Materials Project[56] id: mp-17 173), *Rh$_{17}$S$_{15}$ (ICSD: 410 838, mp-21 991).

**ADVANCED
SCIENCE NEWS**

www.advancedsciencenews.com

**small
structures**

www.small-structures.com

was impregnated on silica together with Rh(OAc)$_3$ and the resulting product was heated in a flowing stream of argon at 700 °C in order to synthesize Rh$_{17}$S$_{15}$/SiO$_2$ (10 wt% Rh). Whereas an excess of 20 and 50 mol% of thiourea resulted in the formation of metallic Rh nanoparticles and nanoparticles of the Rh$_2$S$_3$ phase, respectively, 30 mol% excess led to the formation of the phase-pure Rh$_{17}$S$_{15}$/SiO$_2$ nanoparticles on silica (Figure 1b and S1, Supporting Information). Beside the amount of sulfur precursor, also the temperature of the thermal treatment (Figure S2, Supporting Information) and the gas flow rate (Figure 1c) have shown to be relevant parameters for the synthesis. Rh$_2$S$_3$/SiO$_2$ (10 wt% Rh) was synthesized in a similar manner again via incipient wetness impregnation and a subsequent thermal treatment in a flowing stream of Ar (450 Nl/h) at 700 °C with 50% excess thiourea (with respect to the required stoichiometric ratio) to ensure the phase formation (Figure 1a). The catalyst materials, as described earlier, were also prepared with a lower absolute metal loading (1 wt% Rh) to allow for a reduced size of the nanoparticles through limited sintering processes.

The phase purity of Rh$_{17}$S$_{15}$/SiO$_2$ (10 wt% Rh) and Rh$_2$S$_3$/SiO$_2$ (10 wt% Rh) can be verified by powder X-ray diffraction (PXRD, Figure 1b), whereby the occurrence of very broad reflexes already indicates the formation of small Rh-S crystallites. Subsequently, selected area electron diffraction (SAED) measurements in association with transmission electron microscopy (TEM) were performed for a detailed analysis and provided evidence of Rh$_{17}$S$_{15}$ and Rh$_2$S$_3$ nanoparticles, respectively, supported on silica (Figure S9 and S10, Supporting Information). Despite the fact that PXRD and SAED measurements can be applied for the analyses of the 10 wt% loaded samples, the analyses of the samples resulting from a 1 wt% Rh loading, were found to be challenging due to the very small crystallite/particle sizes of the resulting rhodium sulfides particles (Figure S3, Supporting Information). Interestingly, when Rh/SiO$_2$ (1 wt% Rh) as a reference system was prepared and analyzed via PXRD, reflexes corresponding to metallic Rh particles of comparatively large crystallite size can be identified despite the low metal loading (Figure S4, Supporting Information). This already indicates the role of sulfur as an inherent stabilization agent against sintering processes. The elemental composition and integrity of all samples of rhodium sulfides, could, however, be proven by elemental mapping via energy dispersive X-ray spectroscopy (EDXS), irrespective of whether a high or low Rh loading was chosen. Hereby a uniform Rh and S distribution over the silica support, with Rh/S ratios of 1.13 for Rh$_{17}$S$_{15}$/SiO$_2$ (1 and 10 wt% Rh) and 0.66 for the Rh$_2$S$_3$/SiO$_2$ (1 and 10 wt% Rh, **Figure 2** and S11–S15, Supporting Information), was obtained. Also, the absence of nitrogen-containing species was confirmed and proved the complete decomposition of the thiourea precursor[30,31] and the cleaning of the catalyst surfaces under the applied flowing stream of argon. Lattice fringe distances extracted through high-resolution transmission electron microscopy (HR-TEM) for the Rh$_x$S$_y$/SiO$_2$ samples ($x = 17$, $y = 15$ or $x = 2$, $y = 3$ with 1 and 10 wt% Rh) were well suited with the theoretical d-spacing of the targeted rhodium sulfide phases (Figure S11–S15, Supporting Information).

The morphology of the supported rhodium sulfide nanoparticles could be further explored by TEM. The TEM images of Rh$_x$S$_y$/SiO$_2$ ($x = 17$, $y = 15$ or $x = 2$, $y = 3$ with 1 and 10 wt% Rh) show well dispersed rhodium sulfide nanoparticles on the silica support (Figure S11–S15, Supporting Information) and selected images of Rh$_{17}$S$_{15}$/SiO$_2$ with higher and lower Rh loadings are provided as Figure 2a,b. Almost spherical shaped nanoparticles can be observed in high angle annular dark field scanning transmission electron microscopy (HAADF-STEM) images (Figure S11–S15, Supporting Information) with average particle sizes of 2.2 and 3.0 nm for Rh$_{17}$S$_{15}$/SiO$_2$ and Rh$_2$S$_3$/SiO$_2$ (1 wt% Rh), respectively and 6.3 and 3.6 nm for the 10 wt% loaded analogues. Moreover, the high-resolution HAADF-STEM images of Rh$_{17}$S$_{15}$/SiO$_2$ (10 wt% Rh) through Z contrasting, indicate the formation of a Rh-based surface motif separated spatially by S atoms (Figure 2c,d). The existence of such structural motifs or ensembles on catalysts surfaces has been identified as relevant for active sites of several types of heterogeneous catalysts,[32] whereby the Lindlar catalyst (typically 5 wt% palladium deposited on calcium carbonate or barium sulfate and treated with various forms of lead),[33] is one of the prototypic examples. Combined experimental and theoretical[34] works have shown that through the alloying of Pd with Pb, Pb-induced exclusion areas and consequently separated Pd-rich active sites are being formed.[35] The concept of well-defined structural motifs through formation of crystalline alloys and intermetallic compounds could also be observed for other materials beyond the Lindlar catalyst. Exceptional performance in alkyne semi hydrogenation has been attributed to spatially isolated metal trimers in Pd$_3$S[22] and Ni$_x$P$_y$.[36]

To investigate the oxidation state of Rh within the supported rhodium sulfides, X-ray photoelectron spectroscopy (XPS) analyses of Rh$_x$S$_y$/SiO$_2$ ($x = 17$, $y = 15$ or $x = 2$, $y = 3$ with 1 and 10 wt% Rh) samples were conducted (Figures S19–S23 and Table S1–S3, Supporting Information). The Rh 3d signals were deconvoluted indicating the presence of two types of rhodium species. The doublet at binding energies of 309.5 and 314.4 eV corresponds to 3$d_{5/2}$ and 3$d_{3/2}$ states and can be assigned to rhodium sulfide. This in combination with the S 2p signals, seen in Rh$_x$S$_y$/SiO$_2$ ($x = 17$, $y = 15$ or $x = 2$, $y = 3$ with 10 wt% Rh), at 161.7 and 162.7 eV, corresponding to polysulfides, points toward covalently bound rhodium and sulfur.[24] Further, no S 2p signals at 164 eV were observed, which proves the absence of any elemental sulfur. Another doublet of Rh 3d observed at 307.5 eV (3$d_{5/2}$) and 312.2 eV (3$d_{3/2}$) corresponds to metallic rhodium. The existence of Rh$^{\delta+}$ and Rh^0 species from XPS analyses has also been shown for Rh$_x$P$_y$ systems and can be considered a typical feature for rhodium/p-block element-based phases.[16] The XPS analyses of the low Rh content Rh$_x$S$_y$/SiO$_2$ ($x = 17$, $y = 15$ or $x = 2$, $y = 3$ with 1 wt% Rh) materials have also shown the presence of Rh$^{\delta+}$ and Rh^0, however, no sulfur signals could be observed, due to the very low chalcogenide concentration and potentially reduced surface S concentration. The surface chemistry of the supported Rh$_x$S$_y$ nanoparticles was further explored via diffuse reflectance infrared Fourier transform spectroscopy (DRIFTS) using CO as probe molecule[37] (**Figure 3** and S18, Supporting Information). In the initial DRIFT spectra of the supported rhodium sulfides (Rh$_{17}$S$_{15}$/SiO$_2$ and Rh$_2$S$_3$/SiO$_2$ with 1 wt% Rh) symmetric stretching modes of rhodium gem-dicarbonyl species (Rh^{3+}(CO)$_2$ – a highly oxidized Rh species interacting with two CO molecules) at 2105 cm^{-1} for Rh$_{17}$S$_{15}$ and 2104 cm^{-1} for Rh$_2$S$_3$ and linearly bound CO on metallic Rh (Rh^0-CO)[38,39]
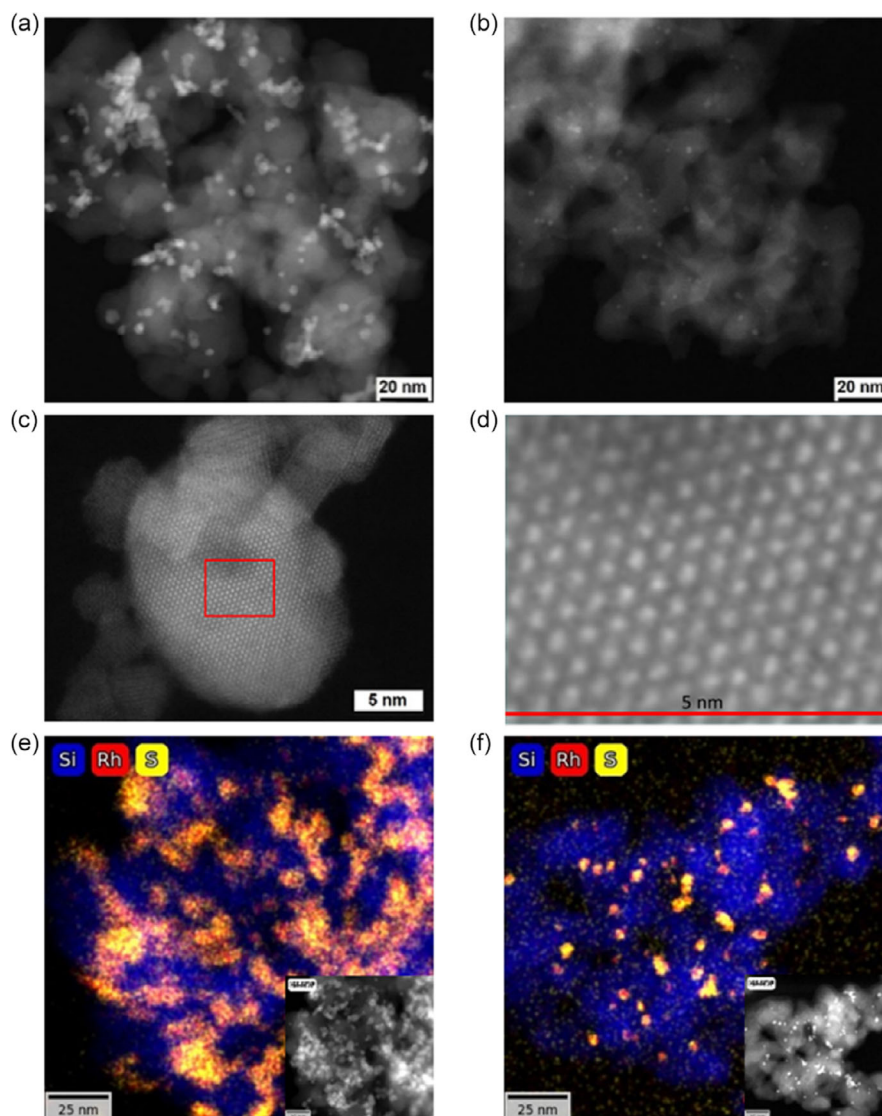
Figure 2. HAADF-STEM images of a) $Rh_{17}S_{15}/SiO_2$ (10 wt% Rh) and b) $Rh_{17}S_{15}/SiO_2$ (1 wt% Rh). c) HR-HAADF-STEM image of $Rh_{17}S_{15}/SiO_2$ (10 wt% Rh) and d) magnified image highlighting the rhodium-containing structural motif. e) EDXS elemental mapping of Rh, S, and Si for $Rh_{17}S_{15}/SiO_2$ (10 wt% Rh) and f) $Rh_{17}S_{15}/SiO_2$ (1 wt% Rh) with corresponding HAADF STEM images at insets.

at 2067 cm^{-1} for $Rh_{17}S_{15}$ and 2073 cm^{-1} for Rh_2S_3 can be assigned. On further exposure to CO, surface reduction of $Rh_{17}S_{15}/SiO_2$ and Rh_2S_3/SiO_2 with 1 wt% Rh is taking place and $Rh^{\delta+}(CO)_2$ symmetric stretching modes can be observed at 2102 cm^{-1} for $Rh_{17}S_{15}$ and 2086 cm^{-1} for Rh_2S_3. In order to elucidate the effect of the sulfur incorporation into Rhodium in more detail, the CO adsorption behavior of Rh/SiO_2 (1 wt% Rh) as reference system was investigated and a blue shift of the symmetric and asymmetric stretches of rhodium gem-dicarbonyl species from pure Rh samples (2098 and 2028 cm^{-1}) to $Rh_{17}S_{15}$ (2102 and 2036 cm^{-1}) can be seen. This finding can be attributed to a charge transfer from Rh to S, also demonstrated by XPS analyses, which leads to an increase in the cationic nature of the rhodium centers in rhodium sulfides in comparison to the metallic rhodium. The low intensity band observed at

1936 cm^{-1} in Rh/SiO_2 (1 wt% Rh) may correspond to a bridged CO vibration mode on Rh^0. Similar signals in this range are absent in the DRIFT spectra of the rhodium sulfides, which points toward the existence of isolated CO chemisorption sites on the surface,[40] as already indicated from TEM imaging.

The oxidation state and chemical environment of the rhodium sulfide materials were further investigated using X-ray absorption spectroscopy (XAS). The X-ray absorption near edge structure (XANES) measurements (Figure 3d) show that Rh atoms within rhodium sulfides (Rh_xS_y/SiO_2, $x = 17$, $y = 15$ or $x = 2$, $y = 3$ with 1 wt% Rh) seem to have a very similar oxidation state, that lies between the Rh^{3+} state of bulk Rh_2O_3 and Rh^0 of the bulk Rh reference. This corresponds to an oxidation state of $Rh^{\delta+}$ based on the partial charge transfer from Rh to S, in agreement with XPS and DRIFTS analyses. The characteristic broad

**ADVANCED
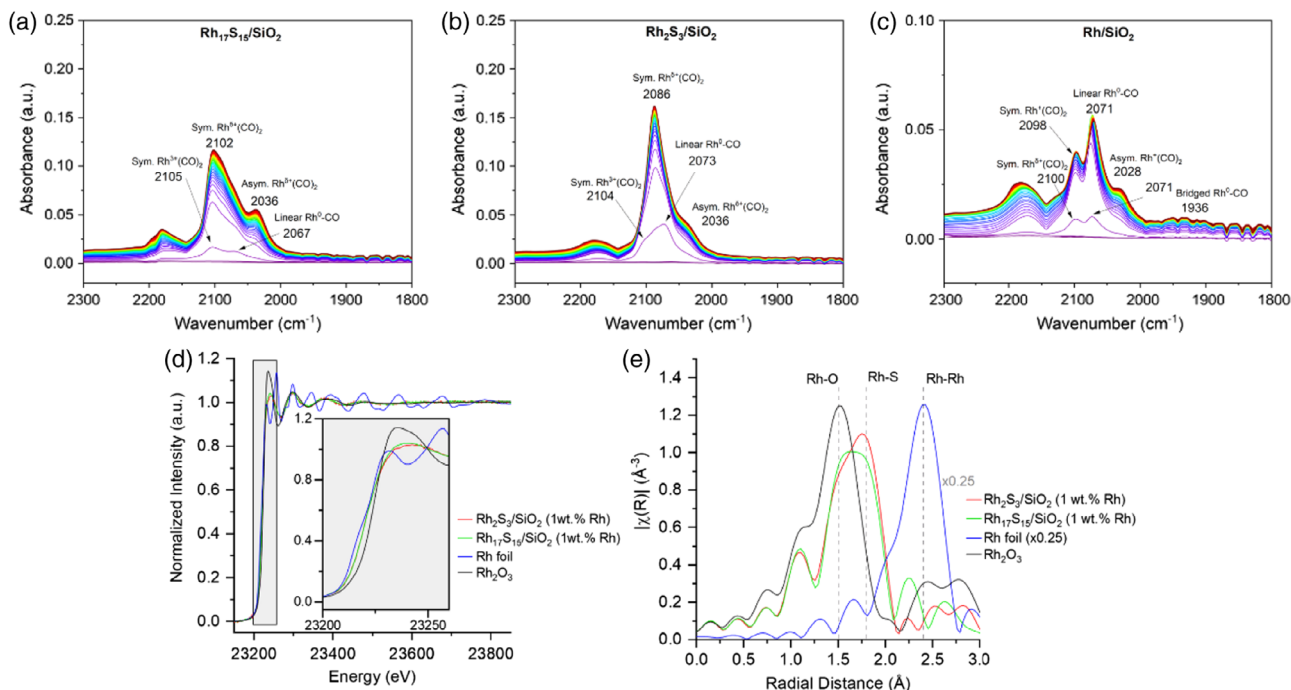SCIENCE NEWS**

www.advancedsciencenews.com

**small
structures**

www.small-structures.com

Figure 3. DRIFT spectra of the synthesized catalyst a) $Rh_{17}S_{15}/SiO_2$ (1 wt% Rh), b) Rh_2S_3/SiO_2 (1 wt% Rh), and c) Rh/SiO_2 (1 wt% Rh) recorded during CO adsorption in 1% CO/Ar (100 mL min^{-1}) at 40 °C. IR bands around 2180 cm^{-1} correspond to gas-phase CO signals. d) Ex situ XAS spectra recorded at the Rh-K edge with an inset showing the XANES region and e) FT-EXAFS spectra (k2-weighted, not phase corrected). As references, the spectra of a metallic Rh foil and a Rh_2O_3 pellet are shown. The contribution at 1.5 Å is most likely due to surface oxidation caused by the sample preparation and prolonged storage in ambient conditions in a capillary prior to the XAS measurements.

white line around 23 240 eV observed in the XANES data was already reported for diverse Rh_xS_y species.[41,42] The corresponding Fourier transform extended X-ray absorption fine structure (FT-EXAFS) spectra are plotted in Figure 3e and prove the existence of rhodium sulfides phases. In addition to the dominant main feature at a backscattering distance (not corrected for scattering phase shift) of 1.8 Å, which resembles Rh-S contributions, a scattering event at a distance of 2.3 Å was observed in $Rh_{17}S_{15}/SiO_2$ (1 wt% Rh), which can be attributed to Rh-Rh scattering events in the $Rh_{17}S_{15}$ crystal structure. The Rh-Rh feature is hereby shifted to lower distances, when compared to the pure Rh metal at 2.4 Å. This finding underlines the more metal-like character of the $Rh_{17}S_{15}$ phase in contrast to the Rh_2S_3 counterpart and undermines the formation of Rh-containing single sites for $Rh_{17}S_{15}$, as shown in Figure 2d.

2.2. Heterogeneous Hydroformylation Catalysis

To assess the catalytic activity of supported rhodium sulfides nanoparticles in the hydroformylation of alkenes, styrene was selected as a model substrate. In this context the modulation of the catalytic selectivity toward the aldehyde products and therewith the reduction of the hydrogenation side reaction is one of the major goals in the development of hydroformylation catalysts.[11] Initial tests were performed using $Rh_{17}S_{15}/SiO_2$ (10 wt% Rh) and Rh_2S_3/SiO_2 (10 wt% Rh) as catalysts under a syngas pressure of 40 bar (CO:H$_2$ 1:1) and a temperature of 80 °C. The conversions of styrene after 80 min of reaction time

using $Rh_{17}S_{15}$ and Rh_2S_3 were 18% and 5% (**Table 1**, entry 1 and 2), respectively. An extended reaction time of 225 min resulted in higher conversions of 85% for $Rh_{17}S_{15}$% and 42% for Rh_2S_3 (Table 1, entry 3 and 4) with traces of (1%) or no hydrogenation products. Subsequently, rhodium sulfide catalysts prepared with 1 wt% Rh loading on silica, were tested under similar reactions conditions. After 80 mins reaction time a styrene conversion of 87% was observed using $Rh_{17}S_{15}/SiO_2$ (1 wt% Rh), whereas

Table 1. Hydroformylation of styrene using different supported rhodium sulfide catalysts.

	Cat.[b]	Rh [wt%]	t [min]	Conv. [%]	Select.[a] [%]	n/iso
1	$Rh_{17}S_{15}/SiO_2$	10	80	18	100	0.7
2	Rh_2S_3/SiO_2	10	80	5	100	–
3	$Rh_{17}S_{15}/SiO_2$	10	225	85	99.3	0.88
4	Rh_2S_3/SiO_2	10	225	42	100	0.7
5	$Rh_{17}S_{15}/SiO_2$	1	80	87	98.4	0.85
6	$Rh_{17}S_{15}/SiO_2$	1	180	100	97.3	1.0
7	Rh_2S_3/SiO_2	1	80	60	98.7	0.85
8	Rh_2S_3/SiO_2	1	120	93	98.6	0.85
9	Rh/SiO_2	1	80	40	98.8	0.91

[a]Selectivity toward aldehyde products. [b]Reaction conditions: 1 mmol styrene, 1.5 mL toluene, 0.2 mol% catalyst, 40 bar syngas pressure, CO:H$_2$ 1:1, 80 °C, 1200 rpm stirring speed.

Rh_2S_3/SiO_2 (1 wt% Rh) gave 60% conversion. From the aforementioned results, a superior activity of the metal-rich $Rh_{17}S_{15}$ catalyst in comparison to Rh_2S_3 and a tremendous activity improvement at lower metal loadings can be concluded, which can also be seen from the syngas pressure consumption within the reactor (**Figure 4**c). The enhanced performance of the catalyst with lower Rh loadings may be due to the reduced particle size and resulting higher rhodium dispersion as concluded from the TEM analysis (Figure S7 and S8, Supporting Information). We assume that lower metal loadings in the synthesis lead to a higher dispersion and therefore to an increased number of exposed surface atoms on the support and available active sites. The conversion versus time plot (Figure 4d) also clearly emphasizes the better performance of $Rh_{17}S_{15}/SiO_2$ (1 wt% Rh) in terms of activity. A reaction time of 3 h using $Rh_{17}S_{15}/SiO_2$ (1 wt% Rh) as a catalyst resulted in 100% conversion of styrene (Table 1, entry 6) with an n/iso ratio of 1.0 and a hydrogenation product (ethyl benzene) concentration of only 2.7%. The regioselectivity might be tunable via the addition of ligands[5] or the use of confinement effects[43] in the future. The catalytic activity of pure Rh on silica (1 wt% Rh) was investigated as reference point and it could be shown that both rhodium sulfide-based catalysts show superior catalytic activity with an order of activity as follows: $Rh_{17}S_{15} > Rh_2S_3 > Rh$. Although the particle size significantly affects the catalytic performance, the primary factor explaining the activity difference between the rhodium sulfides and the pure Rh-based reference catalysts is the electronic contribution from the sulfur incorporation into the rhodium matrix (Figure S31, Supporting Information).

The turnover frequency (TOF) values for the hydroformylation of styrene at 80 °C and 40 bar syngas pressure were estimated as $2620\,h^{-1}$ for $Rh_{17}S_{15}/SiO_2$ (1 wt% Rh) and $1450\,h^{-1}$ for Rh_2S_3/SiO_2 (1 wt% Rh). These estimations were performed based on the metal dispersion calculated by using the average particle diameter obtained from TEM imaging (Table S10, Supporting Information). A comparison of TOF values under similar reaction conditions has shown a superior TOF value for $Rh_{17}S_{15}/SiO_2$ ($2620\,h^{-1}$, 1 wt% Rh) in comparison to Rh_2P/SiO_2 ($1469\,h^{-1}$)[16] and $Rh_7Co_1P_4/SiO_2$ ($2563\,h^{-1}$),[44] underlining the advanced performance of our lead catalyst candidate (Table S10, Supporting Information and Figure 4f).

To broaden the application scope of the catalysts, also with respect to industrially relevant conditions, hydroformylation reactions without additional solvent were carried out. Hereby it was found that by using the lead catalyst candidate $Rh_{17}S_{15}/SiO_2$ (1 wt% Rh) 40% conversion could be achieved in neat styrene after 120 min (Table S7, Supporting Information). Further, the substrate scope was extended, and $Rh_{17}S_{15}/SiO_2$ (1 wt% Rh) has shown to be active in the hydroformylation of 1-hexene, 1-octene, 2-octene, allyl benzene, and diisobutylene displaying excellent activities and selectivity's toward aldehydes (Table S6, Supporting Information).

To explore the recyclability of the supported rhodium sulfide catalysts, $Rh_{17}S_{15}/SiO_2$ (1 wt% Rh) and Rh_2S_3/SiO_2 (1 wt% Rh) were recovered after the hydroformylation reaction by centrifugation and were reused in the hydroformylation of styrene. This recovery confirmed the reusability of the catalysts, as almost no decline in activity or selectivity (n/iso consistently in the range

0.85–0.9) was observed for the catalysts even after two rounds of recycling (Figure S32, Supporting Information). With $Rh_{17}S_{15}/SiO_2$ (1 wt% Rh) providing a reaction time of 80 min, a styrene conversion of 87% was observed with the fresh catalyst and a slightly higher conversion of 94% in the second round of recycling. This trend was confirmed by the determination of the TOF values (Table S11, Supporting Information). Similarly, after a reaction time of 120 min using the fresh Rh_2S_3/SiO_2 (1 wt% Rh) catalysts a conversion of 93% could be achieved, whereas 97% of styrene conversion were obtained in the second round of recycling. However, ICP AES analyses of the recovered catalyst showed a Rh loss (from 1.02 wt% to 0.78 for $Rh_{17}S_{15}/SiO_2$, 1 wt% Rh and from 0.88 to 0.73 wt% for Rh_2S_3/SiO_2, 1 wt% Rh, Table S12, Supporting Information), which points towards leaching induced by mechanical milling and subsequent rhodium sulfide colloid formation. Similar observations were made for other Rh-based hydroformylation catalysts.[45] To improve the anti-leaching performance of our $Rh_{17}S_{15}$-based lead catalyst, $Rh_{17}S_{15}$ (1 wt% Rh) was deposited on alumina and phosphorus-modified silica[19] to enhance metal-support interactions (Table S12, Supporting Information). A substantial reduction in leaching of rhodium to 6% could be observed in the case of $Rh_{17}S_{15}/Al_2O_3$. The catalyst stability was even further improved, with a very low metal loss of 3%, when $Rh_{17}S_{15}$ was deposited on 0.5 P-SiO$_2$ (0.5 wt% P on silica), which demonstrates the potential of support engineering in the field of heterogeneous catalysis. However, a reduction in catalytic activity was observed in both cases, indicating the need for further optimization of the support choice[46] or the use of protectants.[47] In addition to the elemental analyses of postreaction samples, the recovered catalysts were also analyzed via TEM imaging to identify if any changes have occurred to the particles during the catalytic reaction (Figure S16 and S17, Supporting Information). The HAADF-STEM images (Figure S17 and S16, Supporting Information) of the recovered $Rh_{17}S_{15}/SiO_2$ (1 wt% Rh) and Rh_2S_3/SiO_2 (1 wt% Rh) samples showed well dispersed rhodium sulfide nanoparticles on the silica support. Lattice fringe d-spacing of 0.227 nm in line with $Rh_{17}S_{15}$ (331) and 0.259 nm corresponding to Rh_2S_3 (112) were extracted for the recovered $Rh_{17}S_{15}/SiO_2$ (1 wt% Rh) and Rh_2S_3/SiO_2 (1 wt% Rh) catalysts from the HRTEM images (Figure S17 and S16, Supporting Information) and indicate the stability of Rh_xS_y phases after the catalysis. The particle sizes, determined via TEM imaging with the aim to identify sintering or aggregations, revealed a slight increase in the average particle size for the recovered $Rh_{17}S_{15}/SiO_2$ sample (1 wt% Rh) and substantial decrease in the case of Rh_2S_3/SiO_2 (1 wt% Rh, Table S13, Supporting Information). The stability of the phase, besides a minor loss in crystallinity, was also proven be PXRD analyses of the recovered 10 wt% Rh loaded $Rh_{17}S_{15}$ and Rh_2S_3/SiO_2 catalysts (Figure S5, Supporting Information). XAS measurements performed for the recovered Rh_xS_y/SiO_2 ($x = 17$, $y = 15$ or $x = 2$, $y = 3$ with 1 wt% Rh) catalysts still indicates the $Rh^{\delta+}$ oxidation state based on the analyses of the XANES region (Figure S24, Supporting Information). However, especially in the case of the sulfur-rich phase Rh_2S_3, the backscattering contribution at 2.3 Å in the FT-XAFS spectra has increased (Figure S25, Supporting Information). This could imply a loss of sulfur and the partial phase transition from Rh_2S_3 into
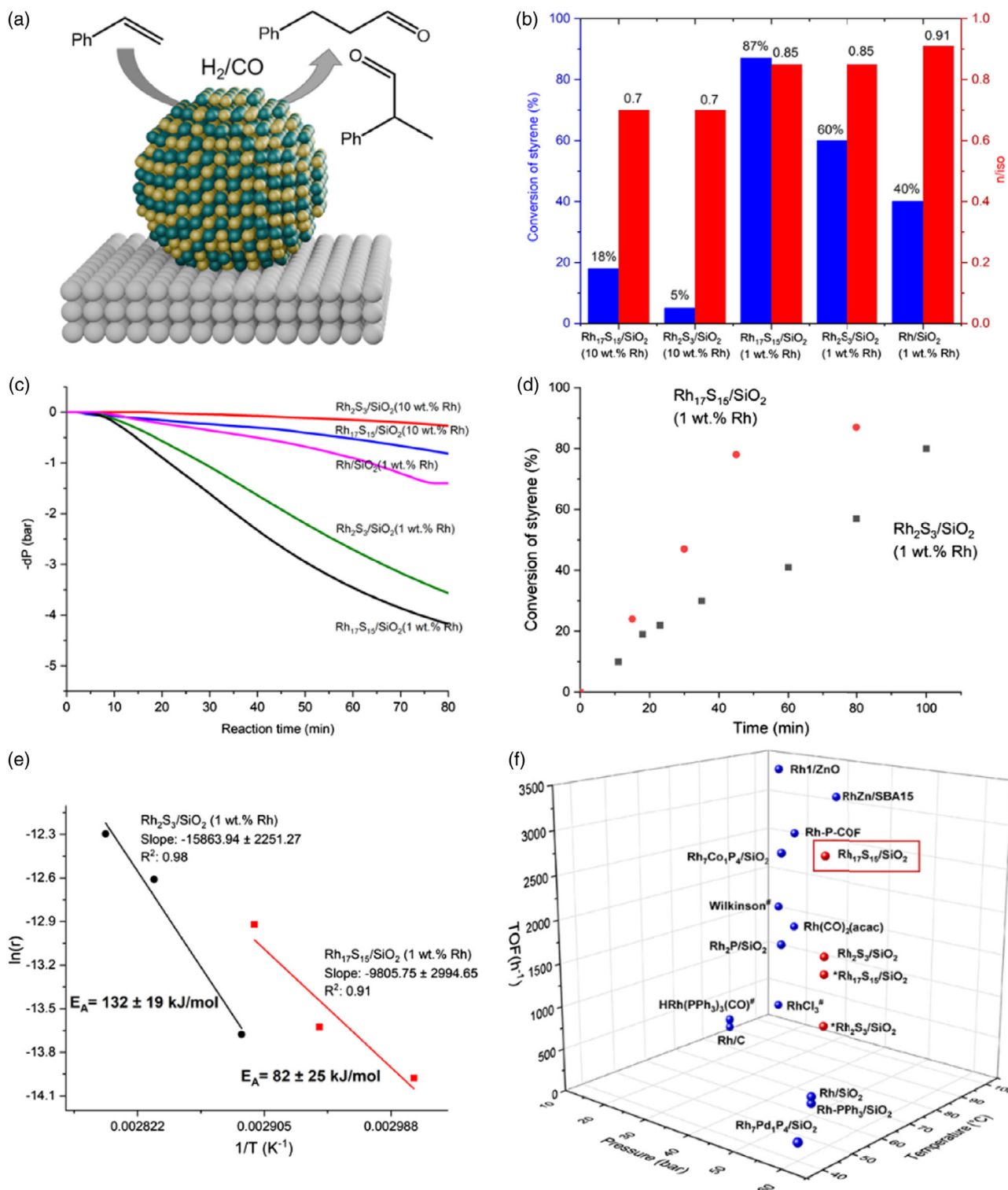
Figure 4. a) Schematic representation of styrene hydroformylation using silica-supported rhodium sulfide catalysts (red: Rh, yellow: S), b) chart showing the conversion and selectivity after 80 min reaction time, c) pressure loss of synthesis gas inside the reactor at 80 °C, d) conversion versus time plot using Rh_xS_y/SiO_2 ($x = 17$, $y = 15$ or $x = 2$, $y = 3$ with 1 wt% Rh) catalysts at 80 °C, e) Arrhenius plots for the estimation of the apparent activation energy with Rh_2S_3/SiO_2 (1 wt% Rh) and $Rh_{17}S_{15}/SiO_2$ (1 wt% Rh) as catalysts. Hydroformylation reaction conditions: 1 mmol styrene, 1.5 mL toluene, 0.2 mol% catalyst, 40 bar syngas pressure, CO: H_2 1:1, 1200 rpm stirring speed. f) Schematic representation of the comparison of various turnover frequency (TOF) values reported for different heterogeneous hydroformylation catalysts applied in the hydroformylation of styrene.[3,12,16,44,57–60] *Estimation based on total Rh content. #Homogeneous catalyst.
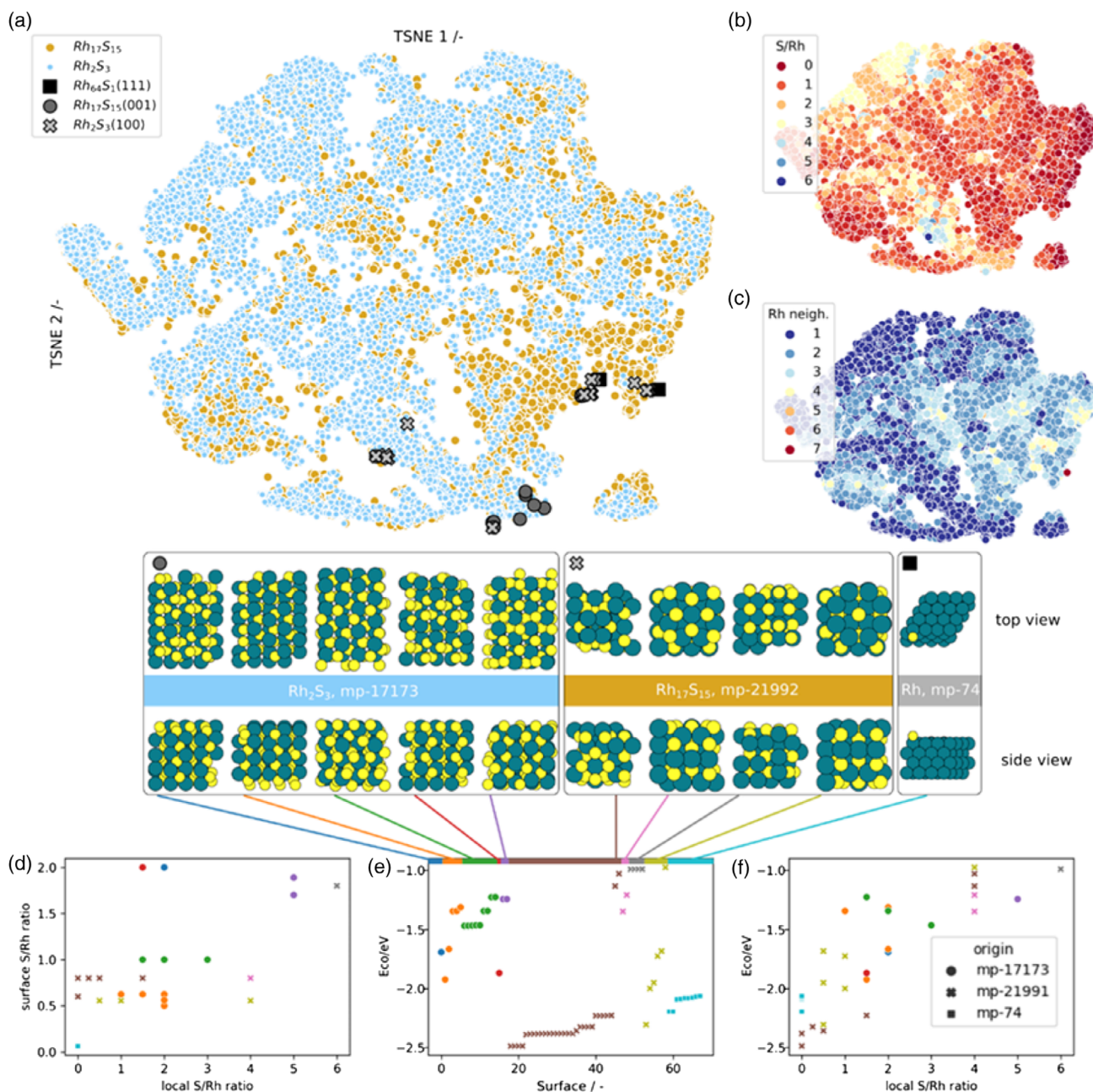
Figure 5. t-SNE derived two-dimensional map based on the SOAP representation of the (a sample of 20.000 representatives chosen from 240.000 options) enumerated sites on all terminations for all crystallographic directions up to miller index = 3 for $Rh_{17}S_{15}$ (mp-21 991) and Rh_2S_3 (mp-17 173). Each point in the map represents a possible active site and close proximity of the points indicate structural similarity of the active sites. As absolute distance between the points are not very meaningful in such analysis, the axis scales are removed as per convention.[52,54,61] a) coloured by the material origin b) coloured by the S to Rh ratio of atoms in a 3 Å radius of the site; c) coloured by the number of Rh atoms in a 3 Å radius of the site; d) ratio of the number of surface atoms of S/Rh versus the local (within 3 Å of the adsorbate contact atom) S/Rh ratio; e) CO adsorption energy (ECO = E * CO–ECO–E*) plotted as a function of origin; f) CO adsorption energy plotted as a function of local composition. Inset bellow: top and side view of (100) $Rh_{17}S_{15}$ (mp-21 991), (001) Rh_2S_3 (mp-17 173), and S-doped (111) Rh (mp-74) surfaces with different terminations. Rh (S) atoms shown as blue (yellow) spheres.

$Rh_{17}S_{15}$, which can also explain the slightly enhanced performance of the recovered Rh_2S_3/SiO$_2$ (1 wt% Rh) catalyst in comparison to the fresh catalyst during the catalyst recycling study (Figure S32c, Supporting Information). On the contrary, the crystallinity of the $Rh_{17}S_{15}$ and Rh_2S_3 samples could have been affected to a different degree.

2.3. Predicting Structural Motifs

To gain a deeper understanding of the exceptional performance of the synthesized catalysts, we employed atomistic simulations. Initially, we focused on investigating the atomic-scale structural differences between the three main active phases: $Rh_{17}S_{15}$, Rh_2S_3, and Rh. The structure of metallic rhodium is well-established (cubic close-packed), and its surfaces have similar metal centers in close spatial proximity allowing for interactions between reaction intermediates on neighboring sites. This property can lead to compromises in the catalyst performance.[33]

In comparison to pure metallic rhodium, we find that both S-containing materials exhibit substantial structural diversity. By exhaustively enumerating all surface terminations up to the third Miller indices and identifying potential high symmetry adsorption (active) sites (using CATKIT)[48] for both $Rh_{17}S_{15}$ and Rh_2S_3 we find over 240 000 among the 2014 possible surface terminations. To visually depict the structural diversity among active sites, we generated Smooth Overlap of Atomic Positions (SOAP)[49,50] descriptors for each identified site, considering a 3.0 Å cut-off distance (approximately one nearest neighbor) followed by a non-linear dimensionality reduction in the descriptor space (T-distributed Stochastic Neighbor Embedding: t-SNE)[51] to derive a two-dimensional visual representation (**Figure 5**a–c).[52–55] By color-coding the representation based on the origin, S/Rh ratio, and Rh content, we discerned the existence of both Rh-rich and Rh-poor sites for both materials within the S/Rh ratio range of 1–6. We observed non-overlapping domains, indicating that while most sites (categorized by their structural similarity) can exist on both materials, there are distinct differences. Therefore, our subsequent efforts are focused on identifying and elucidating these disparities between the two materials.[52–55]

To conduct a quantitative assessment of the energetics associated with the multitude of potential catalytic surfaces, we employed density functional theory (DFT, SI: Computational Details). Although DFT is the standard tool in computational heterogeneous catalysis, due to its cost it enforces limits on the number of configurations that can be sampled. This can lead to significant under-sampling even on simple and particularly on complex materials, such as Rh_xS_y (Figure 5a). To overcome this limitation, we postulate that the local composition of a site predominantly determines its chemical affinity, and focus our attention on the most stable crystallographic directions,[25] (001) for Rh_2S_3 and (100) for $Rh_{17}S_{15}$. Remarkably, these selected directions encompass a comprehensive range of local site S to Rh ratios (as depicted in Figure 5b,c). A simple Rh (111) slab with an S add-atom was included as reference material. We consider all Rh containing sites for all terminations of these facets and find more variety in the local composition of the $Rh_{17}S_{15}$ sites that span local S/Rh ratios from ≈0 to 6 as opposed to 1 to 5 in Rh_2S_3 (from excess of S to S depleted, considering first neighbors to the site defined by the number of atoms in a 3 Å radius; covalent radii of Rh: 1.3 Å and S: 1 Å, Figure 5d). Using DFT, we compute the adsorption energy of CO (E_{CO}, one of the substrates of the hydroformylation reaction) to gauge their chemical affinity[14] and find the sites of $Rh_{17}S_{15}$ as outliers of the range (Figure 5e and S34, Supporting Information). Going from a S saturated $Rh_{17}S_{15}$ termination to a S depleted surface we found a notable increase in CO affinity, adsorption energy ranging from ≈−1.3 eV (Figure 5e, purple) to bellow −2.25 eV (Figure 5h, brown), stronger than to the reference S-doped Rh slab (Figure 5e, light blue). In fact, the local site composition appears to have a profound impact on the CO affinity (Figure 5f) where the strongest binding sites were found to be pure Rh sites while the weakest were found to be Rh sites where Rh is surrounded by S. Thus, tuning the surface S/Rh ratio of Rh sulfides unlocks a range of catalysts with distinct substrate affinities, $Rh_{17}S_{15}$ in particular.

In terms of electronic effects (Figure S40, Supporting Information), sulfur states influence the d-band of the Rh_xS_y materials in a predictable way. However, Rh atoms on $Rh_{17}S_{15}$ show a broader Rh (111) - like projected density of states explaining the high CO affinity at low surface S contents. While some terminations of Rh_2S_3 have a relatively high (−1.83 vs −2.37 metallic Rh) d-band centre, both metallic Rh and $Rh_{17}S_{15}$ bind CO more strongly (Figure 5c) indicating the existence of a geometrical contribution to the binding energy. The presence of geometric effects is clearly depicted in Figure S35–S37, Supporting Information, where the mere presence of S in the neighborhood of the active site (substrate) comes with a substantially weaker (≈0.4 eV) interaction. A geometrical feature uncovered on the S poor terminations of the $Rh_{17}S_{15}$ material is the spatial resolution of neighboring Rh_4 sites. While spatially isolated Rh_4 sites have shown to be the most prominent structural motif, other site-isolated Rh-based sites have also been identified in the case of $Rh_{17}S_{15}$ (Figure S36, Supporting Information). In contrast to metallic Rh, where Rh hollow sites are always available, or Rh_2S_3 where "pure" (sites where the adsorbate has only Rh atoms as its first neighbors) Rh hollow sites are non-existent, terminations of $Rh_{17}S_{15}$ poor in S, block all unselective pathways that arrise from direct interations of neighboring hollow sites (Figure S38, Supporting Information).

3. Conclusion

To conclude, the findings of this study demonstrate that supported crystalline nanoparticles of rhodium sulfides serve as exceptional catalysts for the hydroformylation of alkenes in liquid environments. By employing a robust synthesis method and capitalizing on the tunability of the catalytic surfaces of these materials (via the choice of phase composition and the individual surface treatment), we have discovered highly active catalysts that far exceed the performance of several reference Rh catalyst systems. Using unsupervised machine learning, we have expanded the range of potential active sites and determined that the composition of the active site plays a central role in the substrate affinity, striking a balance between geometric and electronic factors. Notably, Rh-rich terminations of $Rh_{17}S_{15}$ enable the formation of highly reactive structure inherent spatially isolated Rh sites with specifically tailored geometric and electronic properties, a fact that is supported by a plethora of analytical evidence. This study showcases the effectiveness and the potential, also on an industrial level, of the d-block/p-block element combination strategy for engineering metal matrices, through the formation of highly catalytically active and site-isolated metal sites via the

introduction of p-block elements. The combined experimental and computational search for structural surface motifs, such as Metal$_4$ sites in Rh$_{17}$S$_{15}$, will open up new avenues in the exploration of alternative heterogeneous single-site catalysts. The extensive parameter space encompassing the selection of metals and p-block elements spanning the entire periodic table, alongside considerations of phase compositions and tailored synthetic methodologies, represents an extensive domain awaiting experimental exploration.

Supporting Information

Supporting Information is available from the Wiley Online Library or from the author.

Acknowledgements

Conflict of Interest

The authors of this article (A.N., E.F., S.D., S.A.S., and S.H.) have applied for a patent relating to contents of this article (Rhodium Sulfides as Hydroformylation Catalysts).

Author Contributions

Arjun Neyyathala: Data curation (lead); Investigation (equal); Writing—original draft (equal). **Edvin Fako**: Investigation (equal); Writing—original draft (equal); Writing—review & editing (equal). **Sandip De**: Methodology (equal); Software (lead); Writing—review & editing (equal). **Daria Gashnikova**: Investigation (supporting); Methodology (supporting). **Florian Maurer**: Investigation (supporting); Methodology (supporting). **Jan-Dierk Grunwaldt**: Validation (equal); Writing—review & editing (supporting). **Stephan A. Schunk**: Conceptualization (equal); Supervision (equal); Writing—review & editing (supporting). **Schirin Hanf**: Conceptualization (lead); Methodology (equal); Writing—original draft (equal); Writing—review & editing (lead).

Data Availability Statement

The data that support the findings of this study are openly available in [Zenodo] at [https://doi.org/10.5281/zenodo.11082359], reference number [11082360].

Keywords

[1] Y. Liu, Z. Liu, Y. Hui, L. Wang, J. Zhang, X. Yi, W. Chen, C. Wang, H. Wang, Y. Qin, L. Song, A. Zheng, F.-S. Xiao, *Nat. Commun.* **2023**, *14*, 2531.

[2] L. Wang, W. Zhang, S. Wang, Z. Gao, Z. Luo, X. Wang, R. Zeng, A. Li, H. Li, M. Wang, X. Zheng, J. Zhu, W. Zhang, C. Ma, R. Si, J. Zeng, *Nat. Commun.* **2016**, *7*, 14036.

[3] J. Amsler, B. B. Sarma, G. Agostini, G. Prieto, P. N. Plessow, F. Studt, *J. Am. Chem. Soc.* **2020**, *142*, 5087.

[4] S. K. Pedersen, H. G. Gudmundsson, D. U. Nielsen, B. S. Donslund, H. C. D. Hammershøj, K. Daasbjerg, T. Skrydstrup, *Nat. Catal.* **2020**, *3*, 843.

[5] P. Gao, G. Liang, T. Ru, X. Liu, H. Qi, A. Wang, F.-E. E. Chen, *Nat. Commun.* **2021**, *12*, 4698.

[6] M. Zhao, C. Li, D. Gómez, F. Gonell, V. M. Diaconescu, L. Simonelli, M. L. Haro, J. J. Calvino, D. M. Meira, P. Concepción, A. Corma, *Nat. Commun.* **2023**, *14*, 7174.

[7] D. Evans, J. A. Osborn, G. Wilkinson, *J. Chem. Soc. A* **1968**, 3133.

[8] S. Hanf, L. A. Rupflin, R. Gläser, S. A. Schunk, *Catalysts* **2020**, *10*, 510.

[9] P. Samanta, A. Solé-Daura, R. Rajapaksha, F. M. Wisser, F. Meunier, Y. Schuurman, C. Sassoye, C. Mellot-Draznieks, J. Canivet, *ACS Catal.* **2023**, *13*, 4193.

[10] X. Zhang, T. Yan, H. Hou, J. Yin, H. Wan, X. Sun, Q. Zhang, F. Sun, Y. Wei, M. Dong, W. Fan, J. Wang, Y. Sun, X. Zhou, K. Wu, Y. Yang, Y. Li, Z. Cao, *Nature* **2024**, *629*, 597.

[11] L. Alvarado Rupflin, J. Mormul, M. Lejkowski, S. Titlbach, R. Papp, R. Gläser, M. Dimitrakopoulou, X. Huang, A. Trunschke, M. G. Willinger, R. Schlögl, F. Rosowski, S. A. Schunk, *ACS Catal.* **2017**, *7*, 3584.

[12] M. Chen, G. Gupta, C. W. Ordonez, A. R. Lamkins, C. J. Ward, C. A. Abolafia, B. Zhang, L. T. Roling, W. Huang, *J. Am. Chem. Soc.* **2021**, *143*, 20907.

[13] C. Galdeano-Ruano, C. W. Lopes, D. Motta Meira, A. Corma, P. Oña-Burgos, *ACS Appl. Nano Mater.* **2021**, *4*, 10743.

[14] Z. Mao, H. Guo, Z. Xie, P. Liu, J. G. Chen, *Catal. Sci. Technol.* **2022**, *12*, 4988.

[15] N. Huang, B. Liu, X. Lan, T. Wang, *Ind. Eng. Chem. Res.* **2020**, *59*, 18771.

[16] B. Liu, N. Huang, Y. Wang, X. Lan, T. Wang, *ACS Catal.* **2021**, *11*, 1787.

[17] B. Liu, X. Lan, Q. Zhong, T. Wang, *ACS Catal.* **2024**, *14*, 757.

[18] A. Neyyathala, F. Flecken, S. Hanf, *ChemPlusChem* **2023**, *88*, e202200431.

[19] A. Neyyathala, F. Flecken, F. Rang, C. Papke, S. Hanf, *Chem. Eur. J.* **2024**, *30*, e202302825.

[20] C. Liu, J. Zhang, H. Liu, J. Qiu, X. Zhang, *Ind. Eng. Chem. Res.* **2019**, *58*, 21285.

[21] Z. Mao, Z. Xie, J. G. Chen, *ACS Catal.* **2021**, *11*, 14575.

[22] D. Albani, M. Shahrokhi, Z. Chen, S. Mitchell, R. Hauert, N. López, J. Pérez-Ramírez, *Nat. Commun.* **2018**, *9*, 2634.

[23] Y. Yang, X. Zhu, L. Wang, J. Lang, G. Yao, T. Qin, Z. Ren, L. Chen, X. Liu, W. Li, Y. Wan, *Nat. Commun.* **2022**, *13*, 2754.

[24] J. Masud, T. Van Nguyen, N. Singh, E. McFarland, M. Ikenberry, K. Hohn, C.-J. Pan, B.-J. Hwang, *J. Electrochem. Soc.* **2015**, *162*, F455.

[25] N. Singh, D. C. Upham, R. F. Liu, J. Burk, N. Economou, S. Buratto, H. Metiu, E. W. McFarland, *Langmuir* **2014**, *30*, 5662.

[26] D. Richards, S. D. Young, B. R. Goldsmith, N. Singh, *Catal. Sci. Technol.* **2021**, *11*, 7331.

[27] L. Jia, X. Tan, T. Yu, J. Ye, *Energy Fuels* **2022**, *36*, 11308.

[28] A. Calafat, J. Laine, *Catal. Lett.* **1994**, *28*, 69.

[29] S. T. Oyama, *Journal of Catalysis*, Academic Press Inc. **2003**, pp. 343–352.

[30] Z. D. Wang, M. Yoshida, B. George, *Comput. Theor. Chem.* **2013**, *1017*, 91.

[31] V. P. Timchenko, A. L. Novozhilov, O. A. Slepysheva, *Russ. J. Gen. Chem.* **2004**, *74*, 1046.

[32] C. Vogt, B. M. Weckhuysen, *Nat. Rev. Chem.* **2022**, *6*, 89.

[33] H. Lindlar, *Helv. Chim. Acta* **1952**, *35*, 446.

[34] F. Studt, F. Abild-Pedersen, T. Bligaard, R. Z. Sørensen, C. H. Christensen, J. K. Nørskov, *Science* **2008**, *320*, 1320.

[35] G. Vilé, N. Almora-Barrios, S. Mitchell, N. López, J. Pérez-Ramírez, *Chem. Eur. J.* **2014**, *20*, 5926.

[36] D. Albani, K. Karajovic, B. Tata, Q. Li, S. Mitchell, N. López, J. Pérez-Ramírez, *ChemCatChem* **2019**, *11*, 457.

[37] B. B. Sarma, J. Jelic, D. Neukum, D. E. Doronkin, X. Huang, F. Studt, J. D. Grunwaldt, *J. Phys. Chem. C* **2023**, *127*, 3032.

[38] G. Srinivas, S. S. C. Chuang, *J. Catal.* **1993**, *144*, 131.

[39] J. W. Niemantsverdriet, *Spectroscopy in Catalysis: An Introduction*, 2nd, Completely Revised ed., Wiley-VCH Verlag, Weinheim **2000**.

[40] F. C. Meunier, *J. Phys. Chem. C* **2021**, *125*, 21810.

[41] J. M. Ziegelbauer, D. Gatewood, A. F. Gullá, M. J.-F. Guinel, F. Ernst, D. E. Ramaker, S. Mukerjee, *J. Phys. Chem. C* **2009**, *113*, 6955.

[42] J. Liang, A. Levina, J. Jia, P. Kappen, C. Glover, B. Johannessen, P. A. Lay, *Inorg. Chem.* **2019**, *58*, 4880.

[43] X. Dou, T. Yan, L. Qian, H. Hou, M. Lopez-Haro, C. Marini, G. Agostini, D. M. Meira, X. Zhang, L. Zhang, Z. Cao, L. Liu, *Nat. Catal.* **2024**, *7*, 666.

[44] B. Liu, Y. Wang, N. Huang, X. Lan, T. Wang, *ACS Catal.* **2021**, *11*, 9850.

[45] T. Li, F. Chen, R. Lang, H. Wang, Y. Su, B. Qiao, A. Wang, T. Zhang, *Angew. Chem., Int. Ed.* **2020**, *59*, 7430.

[46] B. B. Sarma, D. Neukum, D. E. Doronkin, A. R. L. Nilayam, L. Baumgarten, B. Krause, J.-D. Grunwaldt, *Chem. Sci.* **2024**, https://doi.org/10.1039/d4sc02907k.

[47] J. Zhao, Y. He, F. Wang, W. Zheng, C. Huo, X. Liu, H. Jiao, Y. Yang, Y. Li, X. Wen, *ACS Catal.* **2020**, *10*, 914.

[48] GitHub—SUNCAT-Center/CatKit: General purpose tools for high-throughput catalysis, https://github.com/SUNCAT-Center/CatKit (accessed: May 2024).

[49] A. P. Bartók, R. Kondor, G. Csányi, *Phys. Rev. B* **2013**, *87*, 184115.

[50] L. Himanen, M. O. J. Jäger, E. V. Morooka, F. Federici Canova, Y. S. Ranawat, D. Z. Gao, P. Rinke, A. S. Foster, *Comput. Phys. Commun.* **2020**, *247*, 106949.

[51] L. Van Der Maaten, G. Hinton, *J. Mach. Learn. Res.* **2008**, *9*, 2579.

[52] S. De, A. P. Bartók, G. Csányi, M. Ceriotti, *Phys. Chem. Chem. Phys.* **2016**, *18*, 13754.

[53] A. P. Bartók, S. De, C. Poelking, N. Bernstein, J. R. Kermode, G. Csányi, M. Ceriotti, *Sci. Adv.* **2017**, *3*, 1701816.

[54] S. De, F. Musil, T. Ingram, C. Baldauf, M. Ceriotti, *J. Cheminform.* **2017**, *9*, 6.

[55] P. O. Dral, *Quantum Chemistry in the Age of Machine Learning*, Elsevier Inc. **2024**.

[56] A. Jain, S. P. Ong, G. Hautier, W. Chen, W. D. Richards, S. Dacek, S. Cholia, D. Gunter, D. Skinner, G. Ceder, K. A. Persson, *APL Mater.* **2013**, *1*, 11002.

[57] R. Lang, T. Li, D. Matsumura, S. Miao, Y. Ren, Y. Cui, Y. Tan, B. Qiao, L. Li, A. Wang, X. Wang, T. Zhang, *Angew. Chem., Int. Ed.* **2016**, *55*, 16054.

[58] Y. Liu, A. Dikhtiarenko, N. Xu, J. Sun, J. Tang, K. Wang, B. Xu, Q. Tong, H. J. Heeres, S. He, J. Gascon, Y. Fan, *Chem. Eur. J.* **2020**, *26*, 12134.

[59] D. Han, X. Li, H. Zhang, Z. Liu, G. Hu, C. Li, *J. Mol. Catal. A: Chem.* **2008**, *283*, 15.

[60] B. Liu, N. Huang, Y. Wang, X. Lan, T. Wang, *Chem. Eng. J.* **2022**, *441*, 136101.

[61] F. Musil, S. De, J. Yang, J. E. Campbell, G. M. Day, M. Ceriotti, *Chem. Sci.* **2018**, *9*, 1289.